



1 **Improved parameterization of snow albedo in WRF + Noah. Part II:**
2 **Applicability to snow estimates for the Tibetan Plateau**

3 **Lian Liu^{1,2}, Yaoming Ma^{1,2,3,4}, Massimo Menenti^{5,6}, Rongmingzhu Su^{1,2,4}, Nan**
4 **Yao^{1,2,4}, Weiqiang Ma^{1,2,3}**

5 [1] {Key Laboratory of Tibetan Environment Changes and Land Surface Processes,
6 Institute of Tibetan Plateau Research, Chinese Academy of Sciences, Beijing, 100101,
7 China}

8 [2] {LandAtmosphere Interaction and its Climatic Effects Group, State Key Laboratory
9 of Tibetan Plateau Earth System Science, Institute of Tibetan Plateau Research, Chinese
10 Academy of Sciences, Beijing, 100101, China}

11 [3] {CAS Center for Excellence in Tibetan Plateau Earth Sciences, Beijing, 100101,
12 China}

13 [4] {University of Chinese Academy of Sciences, Beijing 100049, China}

14 [5] {State Key Laboratory of Remote Sensing Science, Institute of Remote Sensing and
15 Digital Earth, Chinese Academy of Sciences, Beijing, 100101, China}

16 [6] {Delft University of Technology, Delft, Netherlands}

17 Correspondence to: Y. M. Ma (yyma@itpcas.ac.cn)

18



19 **Abstract**

20 Snow albedo is important to the land surface energy balance and to the water cycle.
21 During snowfall and subsequent snowmelt, snow albedo is usually parameterized as
22 functions of snow related variables in land surface models. However, the default snow
23 albedo scheme in the widely used Noah land surface model shows evident shortcomings
24 in land-atmosphere interactions estimates during snow events on the Tibetan Plateau.
25 Here, we demonstrate that our improved snow albedo scheme performs well after
26 including snow depth as an additional factor. By coupling the WRF and Noah models,
27 this study comprehensively evaluates the performance of the improved snow albedo
28 scheme in simulating eight snow events on the Tibetan Plateau. The modeling results
29 are compared with WRF run with the default Noah scheme and in situ observations.
30 The improved snow albedo scheme significantly outperforms the default Noah scheme
31 in relation to air temperature, albedo and sensible heat flux estimates, by alleviating
32 cold bias estimates, albedo overestimates and sensible heat flux underestimates,
33 respectively. This in turn contributes to more accurate reproductions of snow event
34 evolution. The averaged RMSE relative reductions (and relative increase in correlation
35 coefficients) for air temperature, albedo, sensible heat flux and snow depth reach 27 %
36 (5 %), 32 % (69 %), 13 % (17 %) and 21 % (108 %) respectively. These results
37 demonstrate the strong potential of our improved snow albedo parameterization scheme
38 for snow event simulations on the Tibetan Plateau. Our study provides a theoretical
39 reference for researchers committed to further improving the snow albedo
40 parameterization scheme.

41 **Keywords:** WRF; snow albedo parameterization; turbulent heat and vapor fluxes;
42 Tibetan Plateau

43



44 **1 Introduction**

45 The surface albedo directly determines the proportion of incident solar radiation that is
46 absorbed by the surface, and is an important parameter in climate and land surface
47 models (LSMs) (Sellers et al., 1996). Small changes in surface albedo can affect the
48 energy balance in the land-atmosphere system, and can drive both local and global
49 climate change (Bloch, 1964).

50 Surface albedo changes dramatically during snowfall and snowmelt cycles. Much
51 research has been carried out to identify the factors that influence these changes,
52 including the effects of terrain shielding, altitude, sky conditions, vegetation, and snow
53 properties such as grain size, liquid water content, depth, and impurities (Warren and
54 Wiscombe, 1980; Wiscombe and Warren, 1980; Aoki et al., 2003; Jonsell et al., 2003;
55 Hansen and Nazarenko, 2004; Liang et al., 2005; Wang et al., 2015; He et al., 2018a).
56 This body of research has led to the development of many parameterization schemes
57 for surface albedo (Oerlemans and Knap, 1998; Wang et al., 2007; Bao et al., 2008; Li
58 and Hu, 2009; Gardner and Sharp, 2010; Kuipers Munneke et al., 2011; Malik et al.,
59 2014; Dang et al., 2015; He et al., 2017, 2018b; Meng and Li, 2019; Saito et al., 2019;
60 Wang et al., 2020). Most snow albedo parameterization schemes depend on statistical
61 empirical formulas and constant parameters, rather than representing physical snow-
62 albedo feedback processes. To improve the performance of snow albedo
63 parameterization schemes for simulating land-atmosphere interactions, Bao and Lyu
64 (2009) added consideration of solar zenith angle to a regional climate model, which
65 resulted in a 1.2 °C temperature increase, and considerably improved the cold bias in
66 East Asia and improved the representation of diurnal ground temperature changes in
67 northwest China. Park and Park (2016) investigated the effect of vegetation on snow
68 covered surface albedo and improved the winter surface albedo estimates from their
69 LSM by including leaf and stem indices in the snow albedo parameterization scheme,
70 which reduced the root mean square error (RMSE) by 69 %. Zhong et al. (2017)
71 considered aerosol radiative effects on snow processes in their simulations and



72 successfully reproduced the snow albedo and snow depth. Fresh snow albedo depends
73 on snow depth, and albedo parameterization schemes that fail to account for this
74 generally overestimate the snow depth. To address this, Wang et al. (2020) developed a
75 new albedo scheme for fresh snow, which accounts for the relationship between fresh
76 snow albedo, snow grain size and snow depth, resulting in improved snow depth
77 estimates during the snow ablation period on the Tibetan Plateau. This highlights the
78 importance of accounting for the effect of snow depth on fresh snow albedo.

79 A coupled land-atmosphere model can provide useful insights into conditions on the
80 Tibetan Plateau, where the terrain is complex and there are few, and unevenly
81 distributed observation stations (Maussion et al., 2011; Yuan et al., 2016; Norris et al.,
82 2017; Bonekamp et al., 2018; Rahimi et al., 2019). However, the parameterization
83 scheme for surface albedo in the Noah LSM, which is currently the most widely used
84 LSM, does not account for all the factors that influence albedo. It includes many
85 predetermined parameters and an approximate treatment of vegetation, soil and snow,
86 which can result in some inaccuracies in the estimated surface albedo (Wen et al., 2011;
87 Liu et al., 2019). For example, the surface albedo parameterization scheme in the Noah
88 LSM considers snow cover and age, but ignores other snow related factors, such as
89 snow depth, that can drive dramatic changes in albedo (Ek et al., 2003). This makes it
90 inappropriate to use the Noah LSM to characterize changes in snow albedo that follow
91 from snowfall and melt processes in complex topographic areas. However, the Noah
92 LSM appears to be the most readily available snow albedo scheme for long term climate
93 modeling research (Rai et al., 2019). Despite its shortcomings, the Noah albedo
94 parameterization scheme does provide substantial improvements to estimates of the
95 magnitude and timing of both the peak snowfall amount and the maximum snow cover
96 extent, following from the scheme's consideration of snow albedo decay and liquid
97 water refreezing (Livneh et al., 2010). The above issues represent opportunities for
98 improvements to be made to the snow albedo parameterization scheme in the Noah
99 LSM.



100 The use of an advanced snow albedo parameterization scheme is crucial for accurate
101 estimation of land-atmosphere interactions over the Tibetan Plateau, where the snow-
102 albedo effect is extremely strong. It has been shown that the Weather Research and
103 Forecasting (WRF; Skamarock et al., 2008) model, when coupled with the default Noah
104 albedo parameterization scheme, results in an apparent cold bias over the Tibetan
105 Plateau (Gao et al., 2015; Meng et al., 2018; Liu et al., 2019). This bias can be reduced
106 by including albedo products from the Moderate Resolution Imaging
107 Spectroradiometer (MODIS) and an additional snow depth parameter as independent
108 variables in the Noah albedo parameterization scheme (Liu, 2020). This approach is not
109 the same as assimilating satellite retrieved snow related products into the LSM, which
110 has also been shown to lead to improvements (Xu and Shu, 2014; Zhang et al., 2014;
111 Lin et al., 2016; Xue et al., 2019). This improved snow albedo scheme has been
112 successfully implemented in the WRF model, coupled with Noah, to simulate land-
113 atmosphere interactions during a regional heavy snow event on the Tibetan Plateau (Liu,
114 2020). However, it has not been shown that the improvements that follow from the
115 improved snow albedo scheme are universal over the Tibetan Plateau, and this should
116 be studied further. Severe snowfall occurs often over the southern Tibetan Plateau,
117 while snowfall over the eastern Tibetan Plateau is generally of relatively weak intensity,
118 and the rate of snowmelt varies widely depending on the heterogeneous underlying
119 surfaces. This makes it necessary to carry out numerical experiments that focus on snow
120 events over the eastern and southern Tibetan Plateau to assess how reliably the
121 improved scheme can be used to characterize different snowfall intensities and
122 snowmelt processes.

123 In this study, we selected eight moderate to snowstorm events that occurred over the
124 southern and eastern Tibetan Plateau to assess the universality of the improvements
125 offered by our improved snow albedo scheme in WRF coupled with the Noah LSM.
126 For each snow event, two numerical experiments were carried out: one implementing
127 the default Noah snow albedo scheme, and the other implementing our improved snow
128 albedo scheme. The model performance was assessed through comparison of the

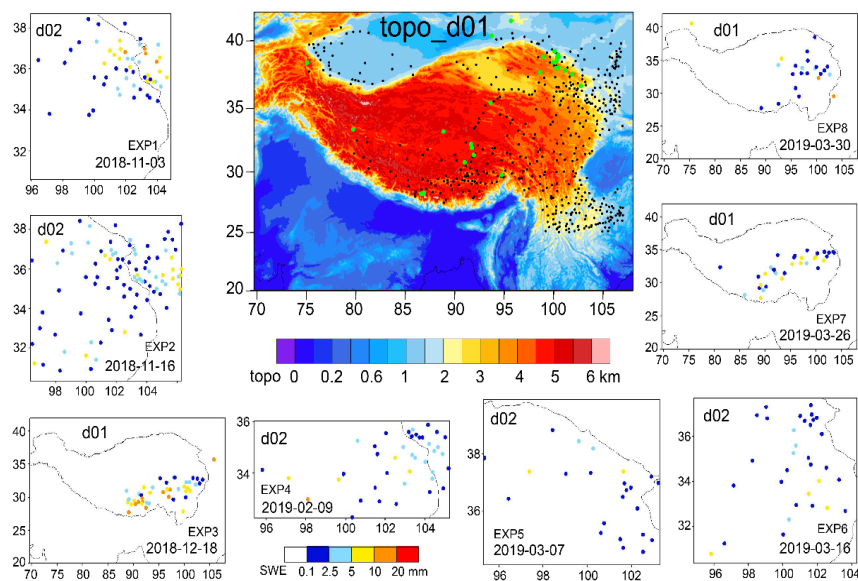


129 modeled air temperature, albedo, snow depth, turbulent heat and vapor fluxes with
130 ground observations. The aim of this study is to explore the potential of our improved
131 snow albedo parameterization scheme to simulate snow events over the whole Tibetan
132 Plateau more accurately than can be done using the standard default scheme. We hope
133 that this study will also provide a useful reference for researchers working to develop
134 and improve this, and other albedo parameterization schemes.

135 **2 Data and methodology**

136 **2.1 Description of snow events**

137 We selected China Meteorological Administration (CMA) national observation stations
138 on the Tibetan Plateau, and in the surrounding regions, with elevations exceeding 1000
139 m. This resulted in a total of 502 stations (Figure 1 shows their distribution). Snowfall
140 events were identified from the hourly air temperature and precipitation observations
141 from all 502 stations when the air temperature was below 0 °C. Daily snowfall amounts
142 were calculated, using 08:00 Beijing Standard Time (BST) as the start and end time for
143 each day. The standards to define snowfall grade were taken from the China
144 Meteorological Standardization Network (<http://www.cmastd.cn/>). Using these
145 standards, eight different grades of snowfall event were considered in our study,
146 including moderate, heavy and snowstorm. Most of the snowfall events took place over
147 the eastern Tibetan Plateau, and some occurred in a large region across the southern and
148 central to the eastern Tibetan Plateau. The maximum daily snowfall amount from all
149 snowfall events exceeded 8 mm, and four events resulted in more than 10 mm daily
150 snowfall, making these snowstorm grade events. Snow depth is much greater on the
151 southern Tibetan Plateau (> 50 cm) than it is on the eastern and central Tibetan Plateau
152 (<=20 cm). The description of eight snowfall events, including the date and location of
153 moderate to snowstorm grade events, the maximum snow depth and daily snowfall
154 amount, are detailed in Table 1. The daily snowfall amounts from the eight snowfall
155 events are shown in Figure 1.



156

157 **Figure 1.** WRF domains of d01 and d02, and CMA observations of daily snowfall
158 amount in color solid circles for the eight experiments. The topographical height of d01
159 is shaded with black solid circles indicating the locations of the CMA stations, and
160 green solid circles indicating the locations of the CAS stations and the Qilian Mountains
161 integrated observatory network.

162

163

164

165

166

167

168

169



170 **Table 1** Description of eight snowfall events using China Meteorological
 171 Administration observations.

Snow events	Event 1	Event 2	Event 3	Event 4	Event 5	Event 6	Event 7	Event 8
Date of moderate to snowstorm	Nov. 3-6, 2018	Nov. 15-17, 2018	Dec. 17-18, 2018	Feb. 9, 2019	Mar. 7-8, 2019	Mar. 16, 2019	Mar. 26, 2019	Mar. 30-Apr. 1, 2019
Region in the Tibetan Plateau	eastern	eastern	southern, central, eastern	eastern	eastern	eastern	southern, central, eastern	central, eastern
Maximum daily snowfall amount (unit: mm)	13.6	9.2	18.7	11	9.3	9.1	8.7	14.3
Maximum snow depth (unit: cm)	18	16	65	20	13	9	53	18

172 **2.2 Model description and experiment configuration**

173 The WRF model (Skamarock et al., 2008), version 3.7.1, coupled with the Noah LSM,
 174 was used to simulate the eight snowfall events in this study. It is a fully compressible,
 175 non-hydrostatic model and includes a run time hydrostatic option. Vertical levels are
 176 determined using a mass based terrain following hydrostatic pressure coordinate, and
 177 calculations are performed on an Arakawa C grid. The model uses 2nd and 3rd order
 178 Runge-Kutta time integration schemes, and 2nd to 6th order advection schemes in both
 179 the horizontal and vertical direction.

180 The extremely steep terrain on the central and southern Tibetan Plateau led to model
 181 instability and failure for snowfall events 3, 7 and 8 when a relatively fine horizontal
 182 resolution of 1 km was used; however, the calculations remained stable when the
 183 resolution was increased to 5 km. We therefore used two two ways nested modeling



184 domains in our model configuration for snowfall events 1, 2, 4, 5 and 6, and a single
185 modeling domain for snowfall events 3, 7 and 8. The coarse domain (d01) was used to
186 simulate synoptic scale atmospheric conditions over 20.0-42.0° N and 69.7-108.0° E
187 with a horizontal resolution of 5 km. The inner domain (d02) had a horizontal resolution
188 of 1 km, and event 1 occupied 876 × 966 grid cells, event 2 occupied 976 × 1001 cells,
189 event 4 was resolved by 966 × 451 cells, event 5 was calculated over 781 × 686 cells,
190 and event 6 covered 926 × 881 cells. The vertical structure of both domains included
191 35 unevenly spaced layers and extended up to 50 hPa. The model was configured to use
192 the Noah LSM in d01 and d02 to describe all land-atmosphere interactions; the
193 Thompson scheme to represent microphysical processes; the Dudhia scheme to
194 represent shortwave radiation, the RRTM scheme to describe longwave radiation; the
195 YSU scheme to describe the planetary boundary layer; and only in d01 to use the Kain-
196 Fritsch cumulus parameterization scheme for clouds.

197 We conducted numerical experiments to simulate snow event 1 (EXP1), event 2 (EXP2),
198 event 3 (EXP3), event 4 (EXP4), event 5 (EXP5), event 6 (EXP6), event 7 (EXP7) and
199 event 8 (EXP8). The model domains for the experiments are shown in Figure 1. Each
200 experiment included two model simulations: one implementing the default Noah snow
201 albedo parameterization scheme, and the other implementing a new improved snow
202 albedo scheme. The snow albedo is parameterized using Eq. (1) and (2) in the default
203 Noah land surface scheme (Livneh et al., 2010), and using Eq. (3) and (4) in the
204 improved scheme (Liu, 2020):

205

$$\alpha_{\text{snow}} = \alpha_{\text{max}} \times A^{t^B} \quad (1)$$

$$\alpha = \alpha_{bg} + sc \times (\alpha_{\text{snow}} - \alpha_{bg}) \quad (2)$$

$$\alpha_{\text{snow}} = 0.13 + 0.66e^{\left(\frac{t}{1.38}\right)} \quad (3)$$

$$\alpha = \alpha_{\text{snow}} + (0.19 - \alpha_{\text{snow}})e^{\left(\frac{-d}{0.11}\right)} \quad (4)$$

208 where A and B are constants, equal to 0.94 and 0.58, respectively, for snow



209 accumulation periods, and are 0.82 and 0.46, respectively, for other periods; α_{bg} is the
210 background albedo, which depends on the land cover type; sc is snow cover, and
211 ranges from 0 to 1; α_{max} is fresh snow albedo; α_{snow} is snow albedo; t is the snow
212 age in units of days; d is snow depth in meters.

213 The fifth generation European Centre for Medium Range Weather Forecasts (ECMWF)
214 reanalysis dataset (ERA5), with a spatial resolution of $0.25^\circ \times 0.25^\circ$ and 3 h temporal
215 resolution, provided initial and boundary conditions for our numerical experiments. The
216 ERA data were calculated using 4DVar data assimilation in CY41R2 from ECMWF's
217 Integrated Forecast System, with 137 vertical hybrid sigma/pressure levels, extending
218 to 0.01 hPa. ERA5 is freely available from the website
219 <https://www.ecmwf.int/en/forecasts/datasets/reanalysis-datasets/era5>. The near real
220 time MODIS land cover product was used to replace the outdated land cover in WRF
221 preprocessing system. We ran the model from before the onset of each snowfall event
222 until and after all snowmelt following the event had ceased. EXP1 was run Nov. 1-8
223 2018, EXP2 was run Nov. 13-18 2018, EXP3 was run Dec. 16-20 2018, EXP4 was run
224 Feb. 5-11 2019, EXP5 was run Mar. 2-10 2019, EXP6 was run Mar. 12-18 2019, EXP7
225 was run Mar. 24-29 2019, EXP8 was run Mar. 28-Apr.7 2019. The model results were
226 output at 3 hours intervals and the first day was used for model spin up.

227 **2.3 Data for model evaluation and comparison**

228 CMA hourly observations of air temperature and snow depth from 502 stations were
229 used to assess the WRF model estimates of 2 m air temperature and snow depth that
230 were made using the improved snow albedo parameterization scheme. Albedo is a key
231 factor for net radiation calculations, and is defined as the ratio of reflected shortwave
232 radiation (upwards) to received shortwave radiation (downwards). It determines the
233 distribution of turbulent land surface heat fluxes between sensible (SH) and latent heat
234 (LH). There are many meteorological observations available that have been
235 continuously recorded on the Tibetan Plateau at atmospheric boundary layer towers,
236 eddy covariance systems (Ma et al., 2018, 2020) and the Qilian Mountains integrated



237 observatory network (Li, 2019; Liu et al., 2020; Zhao and Zhang, 2020). These provide
238 in situ data that are assumed to constitute ‘truth’ for the model validation in this study.
239 In situ observations of albedo, SH and LH from 11 Chinese Academy of Sciences (CAS)
240 stations/samples, and from 16 stations in the Qilian Mountains integrated observatory
241 network are used to evaluate the accuracy of the improved snow albedo
242 parameterization scheme for modeling snow events on the Tibetan Plateau. It is
243 reasonable to compare observations of albedo, SH and LH with model estimates at 5
244 km resolution because there are only a few in situ observation stations in d02, but a
245 total of 27 observation stations in d01. At local solar noon in Lhasa (14:00 BST), the
246 observed albedo value is closer to the Lambertian albedo that is described by the WRF
247 model when coupled with LSMs. We therefore used albedo observations made at 14:00
248 BST to evaluate the model calculated albedo. Quality control codes 1, 2 and 3 were
249 selected when using the Turbulence Knight version 3 (TK3) software, and 0 was used
250 when using the Eddypro software to calculate SH and LH. Details of the 27 stations
251 from the CAS and the Qilian Mountains integrated observatory network that were used
252 in our study are provided in Table 2, and their locations on the Tibetan Plateau are
253 shown in Figure 1. The RMSE and the correlation coefficient were calculated for the
254 comparisons between the observations and the WRF estimates for albedo, air
255 temperature, SH, LH, and snow depth. These are used to assess the performance of the
256 WRF model, when implemented with the default or the improved snow albedo scheme.

257

258

259

260

261

262



263 **Table 2** Location of stations from the Chinese Academy of Sciences (CAS) and the
 264 Qilian Mountains integrated observatory network, and whether or not observations of
 265 albedo, SH and LH were used from each station.

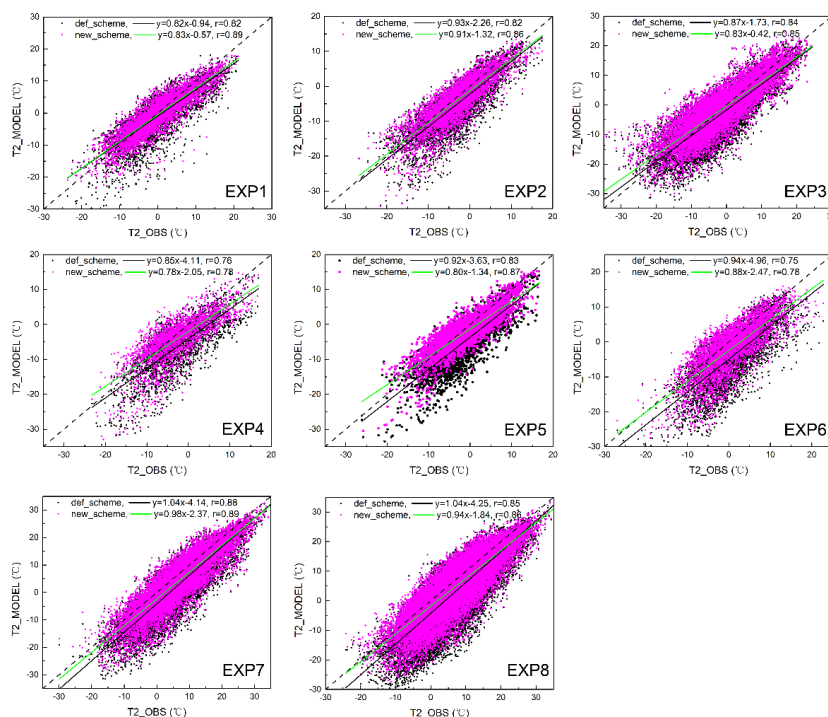
Station No.	Station Name	Station Type	Latitude (° N)	Longitude (° E)	Elevation (m)	Using albedo	Using SH and LH
1	SETS	CAS	29.77	94.73	3326	Yes	No
2	QOMS	CAS	28.21	86.56	4276	Yes	Yes
3	QOMS sample	CAS	28.31	86.85	4600	No	Yes
4	MASWE	CAS	38.41	75.05	3668	Yes	No
5	Nam Co	CAS	30.77	90.99	4730	Yes	Yes
6	NASDE	CAS	33.39	79.70	4264	Yes	No
7	Shuanghu	CAS	33.22	88.83	4947	Yes	Yes
8	NewD66	CAS	35.43	93.59	4465	Yes	No
9	BJ	CAS	31.37	91.90	4509	Yes	Yes
10	MS3478	CAS	31.93	91.71	4620	Yes	No
11	Amdo	CAS	32.24	91.62	4695	Yes	No
12	Yakou	Qilian	38.01	100.24	4148	Yes	Yes
13	Arou	Qilian	38.05	100.46	3033	Yes	Yes
14	Jingyangling	Qilian	37.84	101.12	3750	Yes	Yes
15	Dashalong	Qilian	38.84	98.94	3739	Yes	Yes
16	Heihe Remote Sensing	Qilian	38.83	100.48	1560	Yes	No
17	Huazhaizi Desert Steppe	Qilian	38.77	100.32	1731	Yes	Yes
18	Daman	Qilian	38.86	100.37	1556	Yes	Yes
19	Zhangye wetland	Qilian	38.96	100.45	1460	Yes	Yes
20	Guazhou	Qilian	41.41	95.67	2014	Yes	Yes
21	Dayekou	Qilian	38.56	100.29	2703	Yes	No
22	Dunhuang	Qilian	40.35	93.71	993	Yes	No
23	Liancheng	Qilian	36.69	102.74	2903	Yes	No
24	Linze	Qilian	39.24	100.06	1402	Yes	No
25	Sidalong	Qilian	38.43	99.93	3146	Yes	No
26	Xiyinghe	Qilian	37.56	101.86	3616	Yes	No
27	Tianjun	Qilian	37.70	98.61	3718	Yes	Yes



266 **3 Results**

267 **3.1 Air temperature**

268 Albedo is a key factor in determining the net radiation received at the surface, which
269 determines the land surface energy balance and influences air temperature. Scatterplots
270 of the air temperatures estimated by the WRF model and observed at the CMA stations
271 are shown in Figure 2. In all eight modeling experiments, implementing the improved
272 snow albedo scheme in the WRF model greatly reduces the cold bias that occurs when
273 the default Noah snow albedo scheme is used. Where the default Noah scheme results
274 in a warm bias, however, the improved albedo scheme does not improve the accuracy
275 of the WRF estimates. Scatterplots comparing air temperature observations from CMA
276 station with WRF estimates made using the improved snow albedo scheme estimates,
277 show the data to be concentrated near the ideal fitting line, where the model has exactly
278 reproduced the observations. Using the improved snow albedo scheme results in a
279 marked reduction in the cold bias for the WRF model estimates for EXP1, EXP2, EXP4,
280 EXP5 and EXP6, and the greatest reduction in the cold bias, for all eight experiments,
281 occurs for EXP6 (Fig. 2).



282

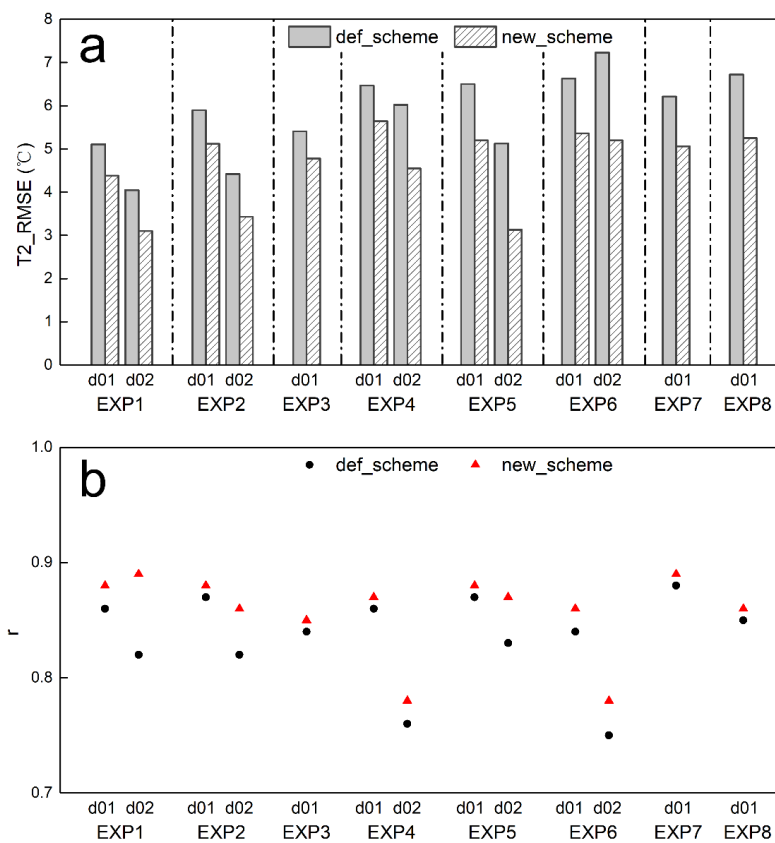
283 **Figure 2.** Scatterplot of air temperature, comparing the CMA observations and model
284 estimates for the eight experiments in the inner (high resolution) model domain from
285 WRF, using the default Noah snow albedo scheme (def_scheme, black solid circle), and
286 using the improved snow albedo scheme (new_scheme, red solid circle). The black
287 solid line is a linear fit to the black solid circles. The green solid line is a linear fit to
288 the red solid circles. The black dotted line is the line $y=x$. r is the correlation coefficient
289 between the CMA observations and the model estimates. The correlation coefficient (r)
290 is significant at 0.01 significance level.

291 To quantify the improvement to air temperature estimates that follows from
292 implementation of the improved snow albedo scheme, the RMSE and correlation
293 coefficient was calculated between CMA observations and model estimates of air
294 temperature, shown in Figure 3. The differences between the accuracy of the new
295 scheme and the default scheme are shown in Table 3. The accuracy of WRF air



296 temperature estimates varies between the different snowfall events, between the
297 different snow albedo schemes, and also varies with model resolution. The lowest air
298 temperature RMSE and the highest correlation coefficient are 3.1 °C and 0.89,
299 respectively, and both occur for EXP1. The highest air temperature RMSE and the
300 lowest correlation coefficient occur for EXP6, reaching 7.2 °C and 0.75, respectively.
301 Air temperature RMSE generally ranges from 4.1 to 7.2 °C for the WRF estimates that
302 were made using the default Noah snow albedo scheme estimates, with correlation
303 coefficients ranging from 0.75 to 0.88. In contrast, when the improved snow albedo
304 scheme is implemented in WRF, the RMSE ranges from 3.1 to 5.6 °C, and the
305 correlation coefficients range from 0.78 to 0.89. Compared with when the default Noah
306 snow albedo scheme is used, the maximum decrease in air temperature RMSE when
307 the new scheme is used reaches 2 °C, which represents an improvement of 39 %, and
308 the average decrease in air temperature RMSE is 1.2 °C, representing an improvement
309 of 20.7 %. There is an improvement of more than 11 % in the RMSE for all eight
310 experiments when the new albedo scheme is used, relative to when the default scheme
311 is used. Implementing the improved snow albedo scheme in WRF for all eight
312 experiments also increased the correlation coefficient between observed and modeled
313 air temperature, by 0.01-0.07, which represents an improvement of 1-9 % (Fig. 3, Table
314 3).

315 Compared with using the default Noah snow albedo scheme, using the improved
316 scheme results in improved model estimates for all eight EXPs, decreasing the air
317 temperature RMSE and increasing the correlation coefficient when compared with
318 observations. These improvements occur for air temperature estimates calculated at
319 both 5 km and 1 km resolution. The improvement to WRF model estimates is greater
320 for calculations made at 1 km resolution than at 5 km resolution, and air temperature
321 estimates are more accurate at 1 km resolution than at 5 km resolution, regardless of
322 which albedo scheme is implemented (Fig. 3, Table 3). Therefore, fine resolution (i.e.,
323 1 km) is strongly recommended for future snowfall event modeling studies.



324

325 **Figure 3.** RMSE (a) and correlation coefficient (b) for air temperature (T2) between
326 observations and model estimates in d01 and d02. The correlation coefficient is
327 significant at the 0.01 significance level. For def_scheme and new_scheme, see Figure
328 2.

329

330

331

332



333 **Table 3** RMSE and correlation coefficient (r) for air temperature between CMA
 334 observations and model estimates, calculated using the default Noah snow albedo
 335 scheme (def_scheme) and the improved albedo scheme (new_scheme). The difference
 336 in RMSE is new_scheme RMSE minus def_scheme RMSE. The difference in r is
 337 new_scheme r minus def_scheme r. P value <0.05 is the significance test for the
 338 correlation.

EXPs	Model Domain	RMSE (°C)			Relative Difference of RMSE	r			
		def_scheme	new_scheme	Difference		def_scheme	new_scheme	Difference	Relative Difference
EXP1	d01	5.11	4.38	-0.73	-14.3 %	0.86	0.88	0.02	2.3 %
	d02	4.05	3.1	-0.95	-23.5 %	0.82	0.89	0.07	8.5 %
EXP2	d01	5.9	5.12	-0.78	-13.2 %	0.87	0.88	0.01	1.1 %
	d02	4.42	3.43	-0.99	-22.4 %	0.82	0.86	0.04	4.9 %
EXP3	d01	5.41	4.78	-0.63	-11.6 %	0.84	0.85	0.01	1.2 %
EXP4	d01	6.47	5.64	-0.83	-12.8 %	0.86	0.87	0.01	1.2 %
	d02	6.02	4.55	-1.47	-24.4 %	0.76	0.78	0.02	2.6 %
EXP5	d01	6.5	5.2	-1.30	-20.0 %	0.87	0.88	0.01	1.1 %
	d02	5.13	3.13	-2.00	-39.0 %	0.83	0.87	0.04	4.8 %
EXP6	d01	6.63	5.36	-1.27	-19.2 %	0.84	0.86	0.02	2.4 %
	d02	7.23	5.2	-2.03	-28.1 %	0.75	0.78	0.03	4.0 %
EXP7	d01	6.21	5.06	-1.15	-18.5 %	0.88	0.89	0.01	1.1 %
EXP8	d01	6.72	5.25	-1.47	-21.9 %	0.85	0.86	0.01	1.2 %

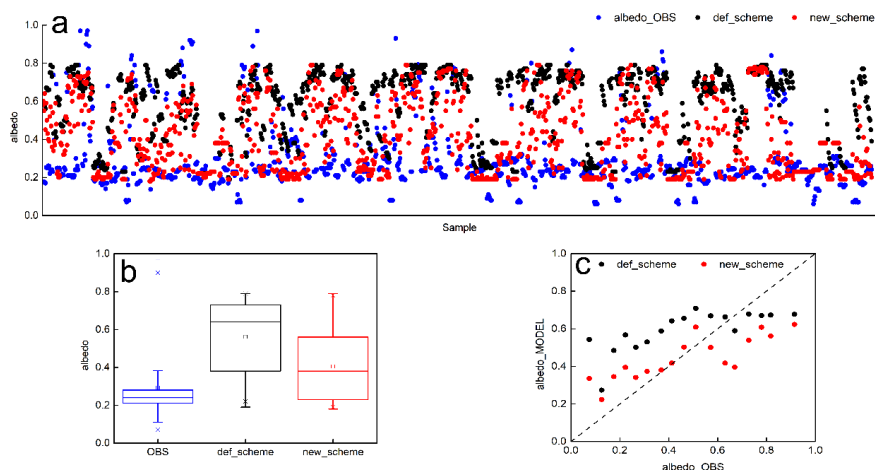
339 3.2 Albedo

340 Using the improved albedo scheme in the WRF model greatly reduces the cold air
 341 temperature bias that otherwise occurs, indicating an improvement to model
 342 performance. It is necessary to compare albedo estimates with in situ observations.
 343 There are very few observation stations located in the finer model domain, and so a
 344 total of 26 stations in d01 were used to evaluate the performance of the WRF



345 simulations of albedo at 5 km resolution (Table 2).

346 Scatterplots comparing observations and WRF estimates for albedo in the eight
347 experiments, when both the default and improved snow albedo scheme were used, are
348 shown alongside our statistical analysis in Figure 4. Albedo higher than 0.7 is
349 interpreted as snowfall. Albedo in the range of 0.4 to 0.6 is interpreted as snowmelt.
350 Albedo lower than 0.3 indicates sparse or patchy snow cover at the in situ stations. For
351 all eight snowfall events, the observed albedo is concentrated at low values, with a
352 median of 0.24, while WRF estimated albedo using the default Noah snow albedo
353 scheme has higher values, with a median of 0.64. Compared with albedo estimates
354 calculated using the default scheme, WRF estimates made using the improved scheme
355 result in a prolonged snowmelt period, which increases the number of snowmelt
356 samples and leads to a median albedo of 0.38, which is closer to that for the in situ
357 observations. The mean albedo estimated from WRF using the improved scheme is 0.4,
358 which is also closer to the observed mean of 0.3, than the mean of 0.6 calculated from
359 WRF using the default scheme (Fig. 4a, 4b). In general, the accuracy of the WRF
360 estimates when the new scheme is used is closely related to the observed albedo.
361 Compared with the WRF estimates made using the default Noah scheme, the WRF
362 estimates made using the improved scheme greatly reduce the overestimation of albedo
363 when the observed values are below 0.6, but seem to increase the underestimation of
364 albedo when the observed values are higher than 0.6 (Fig. 4c).



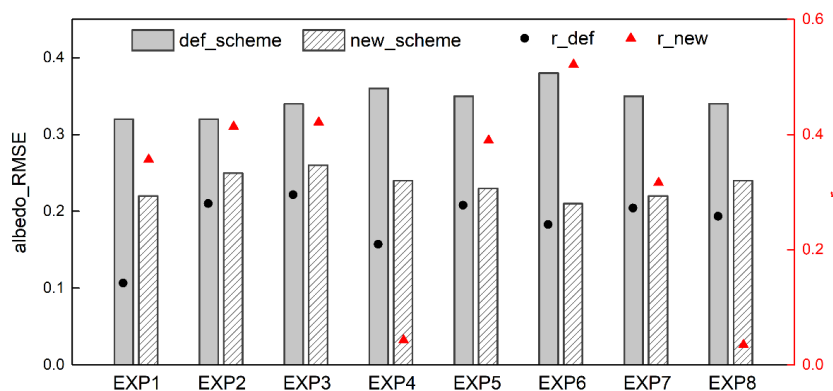
365

366 **Figure 4.** Scatterplot of albedo from observations and model estimates for the eight
367 experiments (a: horizontal axis denotes samples from EXP1 to EXP8), corresponding
368 box-and-whisker plot (b), and averaged observations and model estimates for the eight
369 experiments (c). For def_scheme and new_scheme, see Figure 2.

370 To further evaluate the accuracy of WRF albedo estimates when the different snow
371 albedo schemes are used, we calculated the RMSE and correlation coefficients between
372 the observations and the model estimates (Figure 5). The RMSE for the WRF estimates,
373 when compared to the observations, ranges from 0.32 to 0.38 for the eight experiments
374 when the default scheme is used, and ranges from 0.21 to 0.26 when the improved
375 scheme is used. Compared with the default Noah snow albedo scheme, the improved
376 scheme results in a 0.1 decrease to the albedo RMSE in EXP1, representing a relative
377 decrease of 31.3 %; a 0.07 decrease in EXP2, representing a relative decrease of 21.9 %;
378 a 0.08 decrease in EXP3, representing a relative 23.5 % decrease; a 0.12 decrease in
379 EXP4 and EXP5, representing relative decreases of 33.3 % and 34.3 %, respectively; a
380 0.17 decrease in EXP6, representing a relative 44.7 % decrease; a 0.13 decrease in
381 EXP7, representing a relative 37.1 % decrease; and a 0.1 decrease in EXP8,
382 representing a relative 29.4 % decrease. With the exceptions of EXP4 and EXP8,
383 correlations between the modeled and observed albedo are significant at the 0.01



384 significance level. Implementing the improved albedo scheme in WRF increases the
385 albedo correlation coefficient by 0.21 in EXP1, a relative increase of 151 %; by 0.13 in
386 EXP2, a relative increase of 47.6 %; by 0.13 in EXP3, a relative increase of 42.5 %; by
387 0.11 in EXP5, a relative increase of 40.7 %; by 0.28 in EXP6, a relative increase of
388 114 %; and by 0.04 in EXP7, a relative increase of 16.2 % (Fig. 5). In general, during
389 snowfall and the snowmelt period that follows it, implementing WRF using the
390 improved snow albedo scheme outperforms implementing WRF using the default Noah
391 scheme and results in more accurate albedo estimates, demonstrated by considerable
392 decreases in RMSE and increases in the correlation coefficients.



393

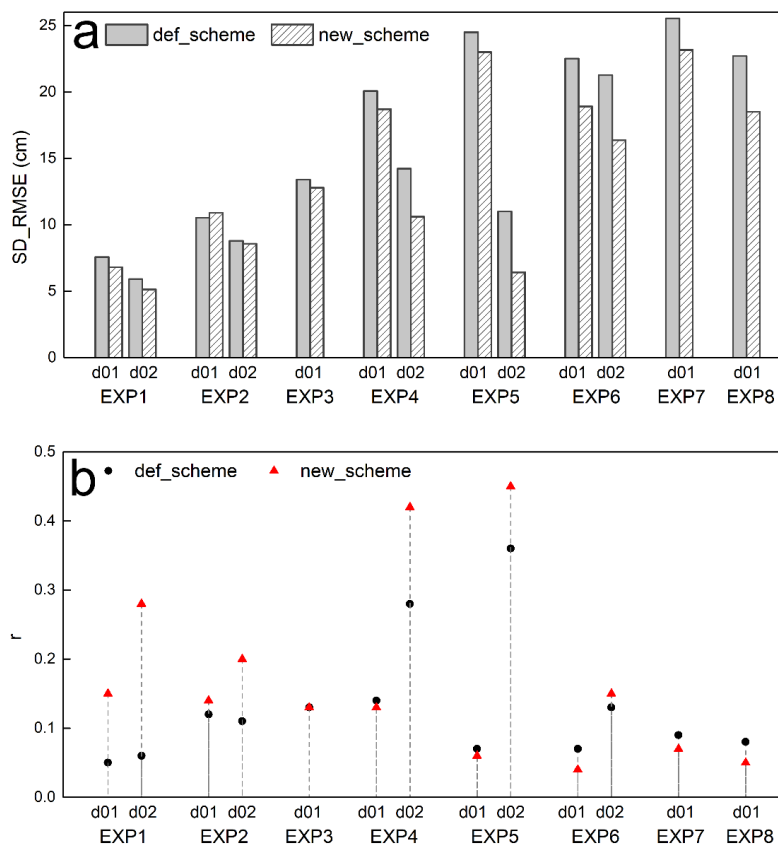
394 **Figure 5.** RMSE in column and correlation coefficient (r) in scatterplot for albedo,
395 comparing observations and model estimates. r_{def} and r_{new} mean r between the
396 observations and WRF-estimates using the default albedo scheme, and using the
397 improved albedo scheme, respectively. Except EXP4 and EXP8, the correlation
398 coefficient is significant at the 0.01 significance level. For `def_scheme` and
399 `new_scheme`, see Figure 2.

400 3.3 Snow depth

401 There is a feedback between albedo and snow. Snow accumulation and snowmelt
402 influence the proportion of solar irradiance that is reflected; albedo indirectly and non-



403 negligibly influences snow accumulation and snowmelt by affecting the land surface
404 energy budget. In this study, we use an improved snow albedo scheme in which albedo
405 is parameterized as a function of snow depth and age. WRF model estimates of albedo
406 calculated using the improved snow albedo scheme outperform those calculated using
407 the default Noah scheme when snowfall events are simulated, and this leads to
408 improved representation of snowfall and the subsequent snowmelt processes in WRF
409 when the improved scheme is used. Instantaneous direct measurements of snow depth
410 are recorded during snowfall events and over the subsequent snowmelt period. We use
411 these to quantify the improvement that using the new albedo scheme makes to snow
412 estimates calculated in WRF. We assess this by calculating the RMSE and correlation
413 coefficient between the model snow depth estimates and CMA observations, as shown
414 in Figure 6.



415

416 **Figure 6.** Same as Figure 3, but for RMSE (a) and correlation coefficient (b) for snow
 417 depth (SD). The correlation coefficient is significant at the 0.01 significance level,
 418 except for d01 estimates in EXP6.

419 Comparing the accuracy of WRF snow depth estimates calculated using the new
 420 scheme, to the accuracy achieved using the default Noah scheme, the greatest relative
 421 decrease in RMSE is 41.7 %, which occurs for estimates made at finer resolution in
 422 EXP5. Replacing the default albedo scheme with the new scheme in WRF results in an
 423 average decrease in snow depth RMSE of 2.2 cm, which is a 13.4 % improvement. In
 424 areas covered by the higher resolution model domain, the average RMSE decrease is
 425 2.8 cm, which is a 21.2 % improvement. This shows that the impact of replacing the



426 albedo scheme with an improved scheme is more significant for areas in the higher
427 resolution d02 model domain than for areas in the coarser d01 model domain (Fig. 6a).
428 Using the improved albedo scheme in WRF increases the correlation coefficient
429 between observed and modeled snow depth in areas within the d02 model domain, but
430 this increase is not consistent for areas in the d01 domain. The greatest increase, both
431 relative and absolute, in the snow depth correlation coefficient occurs in the finer
432 simulation domain in EXP1, where the correlation between observed and modeled
433 snow depth increases by 0.22, which is a 366.7 % increase. The mean and relative
434 increases in the correlation coefficient between observed and modeled snow depth for
435 areas in the d02 simulations are 0.14 and 107.8 %, respectively (Fig. 6b). WRF snow
436 depth estimates are more accurate at finer resolution (i.e., 1 km resolution) than in
437 coarser simulations (i.e., 5 km resolution), regardless of which albedo scheme is
438 implemented (Fig. 6). Implementing the improved albedo scheme in WRF improves
439 the agreement between model estimated and observed snow depth, relative to
440 implementing the default Noah albedo scheme, as seen by the decreased RMSE and the
441 increased correlation coefficient.

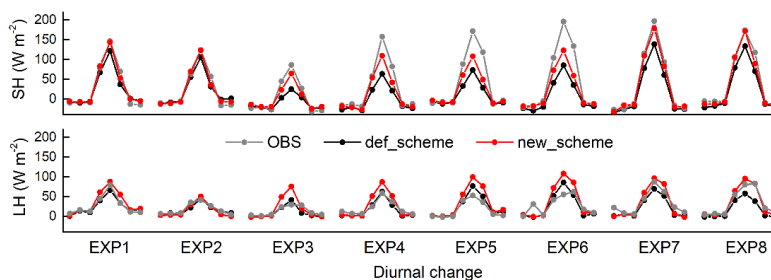
442 **3.4 Turbulent heat and vapor fluxes**

443 Albedo plays a significant role in the land surface energy balance. It determines the
444 proportioning of net radiation fluxes between turbulent heat and vapor fluxes. Our study
445 shows that using the improved snow albedo scheme in WRF results in a good model
446 representation of surface albedo in simulations of snow events. We now consider
447 whether replacing the default scheme with the improved scheme may affect the
448 proportioning of net radiation fluxes between turbulent heat and vapor fluxes. Since
449 there are very few observation in situ stations located in the area covered by the finer
450 model domain, a total of 14 in situ stations located in the area covered by d01 were
451 selected, and WRF estimates of turbulent heat and vapor fluxes were assessed from
452 simulations calculated at 5 km resolution (Table 2)

453 The diurnal changes in SH and LH recorded in the in situ observations and calculated



454 in the eight modeling experiments are shown in Figure 7. The WRF model successfully
455 captures the diurnal changes in SH and LH, particularly in EXP1 and EXP2, where the
456 model estimates of SH and LH are almost equal to the in situ observations. In the
457 nighttime, the WRF model accurately estimates SH and LH in all eight experiments.
458 However, during the day WRF consistently underestimates SH in all experiments
459 except EXP1 and EXP2, and estimates LH with varying accuracy when the default
460 Noah albedo scheme is used. For example, when the default Noah scheme is used, WRF
461 accurately estimates LH in EXP3 and EXP4, but overestimates LH in EXP5 and EXP6
462 and underestimates LH in EXP7 and EXP8. Compared with WRF estimates calculated
463 using the default scheme, WRF simulations calculated using the new albedo scheme
464 result in increased estimates of the turbulent heat and vapor fluxes. This leads to SH
465 estimates that are closer to observations for experiments EXP3 to EXP8, a greatly
466 overestimated LH for experiments EXP3 to EXP6, and a slightly overestimated LH,
467 which is closer to observations for EXP7 and EXP8 (Fig. 7). In general, WRF estimates
468 of SH are improved through the implementation of the new albedo scheme, relative to
469 the default scheme, although SH is underestimated during snowfall events. The impact
470 of the improved albedo scheme on LH estimates varies between the different snowfall
471 events, but LH is consistently overestimated.



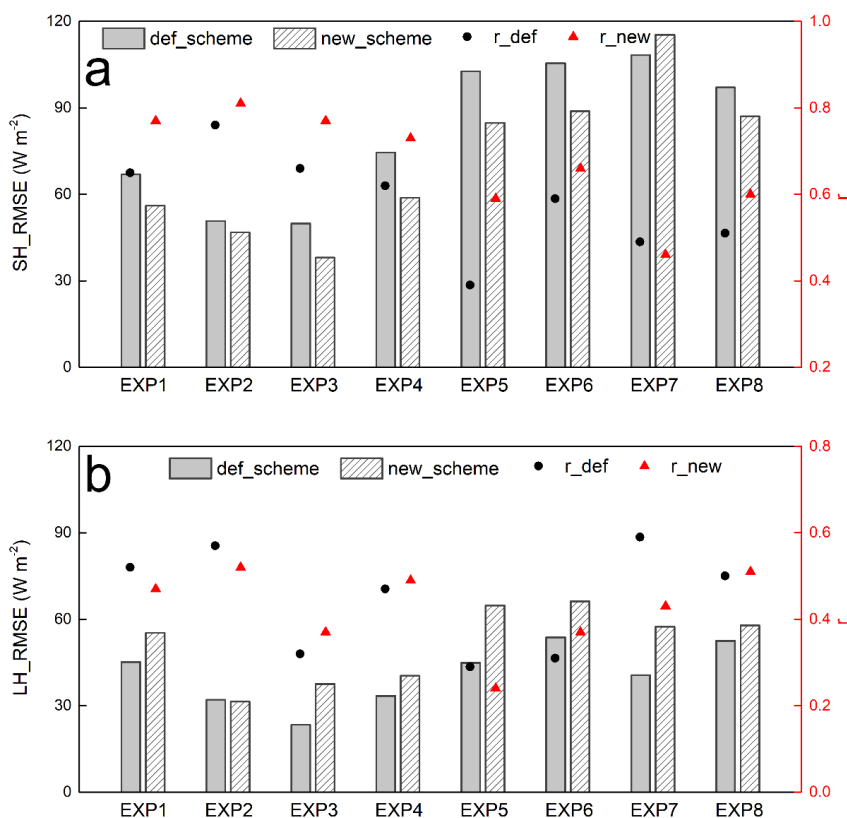
472

473 **Figure 7.** Diurnal change of sensible (SH) and latent (LH) heat fluxes from ground
474 observations and model estimates. Beginning at 02:00 BST with 3 hours interval. For
475 def_scheme and new_scheme, see Figure 2.



476 The RMSE and correlation coefficient for comparisons between WRF estimates and
477 observations for SH and LH are shown in Figure 8. Compared with when the default
478 Noah scheme is used, WRF estimates using the improved scheme result in reduced
479 RMSE for SH estimates in all experiments except EXP7. The absolute (and relative)
480 reductions are: 10.9 W m^{-2} (16.2 %) in EXP1, 3.9 W m^{-2} (7.6 %) in EXP2, 11.9 W m^{-2}
481 (23.8%) in EXP3, 15.7 W m^{-2} (21 %) in EXP4, 17.9 W m^{-2} (17.4 %) in EXP5, 16.6 W
482 m^{-2} (15.8 %) in EXP6, and 10.0 W m^{-2} (10.3 %) in EXP8. There is a relative increase
483 of 6.5 % in EXP7. Implementing the improved scheme in WRF significantly increases
484 the correlation coefficients between observed and modeled SH, relative to using the
485 default scheme, in all experiments except EXP7, where there is a slight decrease. The
486 largest increase in the SH correlation coefficient, both absolute and relative, is 0.2 and
487 51.3 %, respectively, and occurs for EXP5. Implementing the improved scheme in WRF
488 reduces the SH RMSE by an average of 10 W m^{-2} , which is an improvement of 13.2 %
489 improvement, and increases the SH correlation coefficient by an average of 0.1, which
490 is an improvement of 16.8 % (Fig. 8a). However, replacing the default scheme with the
491 improved albedo scheme results in less accurate estimates of LH, and corresponds to
492 an increase in RMSE in almost all eight experiments, although the correlation
493 coefficient increases for half of the snowfall events simulations (EXP3, EXP4, EXP6
494 and EXP8) (Fig. 8b).

495 In summary, the improved snow albedo scheme has a significant effect on the
496 proportioning of radiative fluxes between turbulent heat and vapor fluxes. It
497 significantly outperforms the default Noah scheme in relation to SH estimates, but there
498 is no significant improvement in LH estimates and these may be less accurate when the
499 new scheme is used, relative to the default scheme, during snowfall and the subsequent
500 snowmelt period.



501

502 **Figure 8.** Same as Figure 5, but for sensible (a) and latent (b) heat fluxes. The
503 correlation coefficient is significant at the 0.001 significance level.

504 **4 Discussion**

505 The highly complex topography of the Tibetan Plateau means that WRF estimates of
506 air temperature, albedo and snow depth are strongly sensitivity to model resolution. Our
507 study shows that WRF performs much more accurately when run at finer resolution (1
508 km) than at relatively coarse resolution (5 km) for snowfall events over the Tibetan
509 Plateau, regardless of which snow albedo parameterization scheme is used. This
510 difference may be explained by the ability of the model to resolve complex terrain
511 (Rahimi et al., 2019), and/or by the implementation of the cumulus convective



512 parameterization scheme. The more detailed representation of complex terrain and the
513 explicit representation of convection mean that running WRF at finer resolution greatly
514 improves model estimates of air temperature, surface pressure, and relative humidity
515 (Singh et al., 2020), and provides small improvements in the magnitude of daytime
516 convective precipitation (Collier and Immerzeel, 2015). Norris et al. (2017) pointed out
517 that decreasing the grid spacing from 6.7 to 2.2 km likely improves estimates of
518 mountain precipitation but does not fundamentally change the representation of the
519 diurnal cycle. They indicated that the key difference between low and high model
520 resolution is whether or not a cumulus convective scheme is required. Subkilometer
521 grid resolution has been investigated in WRF, and used for modeling meteorological
522 variables over complex terrain (Horvath et al., 2012; Dimitrova et al., 2016). The 500
523 m resolution configuration of WRF results in the closest match between the model
524 estimates and observations, and gives the most plausible spatial distribution of
525 precipitation over the complex topography. The performance of the WRF model has
526 been similarly demonstrated to improve at 500 m, relative to coarser resolutions, for
527 wind and air temperature estimates (Bonekamp et al., 2018). We therefore strongly
528 suggest that subkilometer grid resolution should be considered when WRF is
529 configured for simulations covering areas in High Mountain Asia in future research.

530 Our improved snow albedo scheme parameterizes albedo as a function of snow depth
531 and age by considering the relationship between MODIS albedo and the modelled snow
532 depth and age. It is more physically plausible than the default Noah scheme, which
533 considers snow cover, and outperforms the default Noah scheme for air temperature,
534 snow depth, albedo and turbulent heat and vapor fluxes estimates during snowfall
535 events. However, even when the improved albedo scheme is used, the RMSE for WRF
536 estimates of albedo at 5 km spatial resolution remains around 0.21-0.26, although this
537 represents a decrease of 22-45 % relative to when the default albedo scheme is used. It
538 should be noted that the accuracy of the MODIS albedo retrieval algorithm is limited
539 during snowfall events and snowmelt periods (Qin et al., 2011; An et al., 2020), and
540 also that rugged mountain terrain not only affects the radiation absorbed by the land



541 surface, but also affects the radiation reflected by the land surface to the satellite borne
542 sensor. Multiple reflection and scattering from adjacent mountains creates challenges
543 for the monitoring and retrieval of surface albedo in areas of complex terrain via remote
544 sensing (Zhang and Gao, 2011; Roupioz et al., 2014, 2016). This reduces the accuracy
545 of MODIS albedo retrieval over the complex topographic Tibetan Plateau and
546 constitutes a limitation to the improved albedo parameterization investigated here, since
547 it relies on MODIS albedo products. A terrain correction is required for the MODIS
548 albedo retrieval to further improve the albedo parameterization scheme used here.
549 However, it is difficult to establish a unified terrain correction model due to the large
550 undulations of the Tibetan Plateau. How to effectively eliminate the influence of terrain
551 factors from a specific mountain surface on quantitative retrievals from remote sensing
552 data has long been a challenge and a focus for remote sensing research. A further
553 challenge for the assessment presented here is the sparse and uneven distribution of
554 available in situ albedo observation data over the bulk Tibetan Plateau. This paucity of
555 data means that there is a mismatch in spatial resolution when comparing albedo
556 estimates, calculated at 5 km resolution, with in situ observations.

557 Air temperature is a critical factor that is related to albedo and determines energy
558 distribution between SH and LH. Using the improved snow albedo parameterization
559 scheme significantly reduces the albedo overestimates during snowfall events that
560 occur when the default scheme is used, and this leads to the reduction of the cold air
561 temperature bias in the model. Therefore, in this study, the improved scheme reduces
562 the underestimates for SH and improves the performance of WRF for simulating SH
563 over the Tibetan Plateau, relative to when the default scheme is used. These results
564 indicate that the accurate simulation of surface albedo is very important for the accurate
565 simulation of SH.

566 Implementing the improved albedo scheme results in little improvement to estimates of
567 LH calculated, which is restricted by water content and increased only slightly, relative
568 to when the default albedo scheme is used. This may be explained by the LH



569 parameterization scheme used in the Noah LSM (Chen and Dudhia, 2001). The total
570 LH in the Noah LSM has three components (LH from the direct evaporation from the
571 top surface layer, evaporation of precipitation intercepted by the canopy and
572 transpiration via the canopy and roots respectively). The factors affecting calculation
573 of LH in the Noah LSM include not only the radiation balance (which is impacted by
574 albedo), but also soil water, soil capillary conductivity and vegetation status, i.e., albedo,
575 surface heat and water vapor exchange coefficient, saturated water vapor pressure,
576 specific humidity, surface soil water content, field capacity, wilting point, canopy
577 resistance, total precipitation, and canopy interception amount. In our current study, we
578 have focused on the snow albedo parameterization scheme in the Noah LSM by
579 considering the MODIS albedo product and the additional snow related variable of
580 snow depth. Therefore, the influence of our improved scheme on LH estimates
581 calculated by the LSM is very limited.

582 Implementing the improved snow albedo scheme in place of the default scheme greatly
583 decreases the overestimation of albedo from snowmelt to snow free processes, but does
584 not remove the underestimation of albedo during snowfall. This means that the
585 improvements mainly come from snowmelt and snow free simulations, and model
586 performance during snowfall may be worse when the improved albedo scheme is used.
587 This suggests an opportunity to further investigate how albedo is characterized by snow
588 depth and age in the snow albedo parameterization scheme.

589 **5 Conclusions**

590 We conducted several numerical experiments to evaluate the performance of the
591 MODIS albedo based snow albedo parameterization scheme (Liu, 2020) implemented
592 in WRF. We assessed the RMSE and correlation coefficient between observed and
593 modeled air temperature, albedo, snow depth and turbulent heat and vapor fluxes for
594 simulations of eight snowfall events over the Tibetan Plateau. We compared the
595 accuracy of WRF estimates made using the improved snow albedo scheme with that of
596 WRF estimates made using the default Noah scheme, in both cases comparing with



597 ground observations.

598 The accuracy of WRF estimates of albedo is significantly improved when the new
599 albedo scheme is implemented. The default Noah scheme tends towards higher albedo
600 estimates and cannot accurately capture snowfall and snowmelt processes, resulting in
601 a high RMSE and low correlation coefficient between modeled and observed albedo.
602 Through consideration of snow related variables, such as snow depth and age, and by
603 being based on MODIS remote sensing albedo products, the improved scheme
604 estimates albedo more accurately than the default scheme, improving the albedo RMSE
605 by around 22 % to 45 %, with an average improvement of 32 %. Similarly, the improved
606 scheme results in an increased correlation coefficient between modeled and observed
607 albedo. Relative to the default scheme, the correlation coefficient relatively increases
608 by around 16 % to 151 %, with an average improvement of 69 %. This may contribute
609 to the relatively better performance of WRF for simulating air temperatures when the
610 improved albedo scheme is used. The improved scheme relatively decreases (increases)
611 the air temperature RMSE (correlation coefficient) by 16 % (1.5 %) for model estimates
612 calculated at 5 km resolution, and by 27 % (5 %) for model estimates calculated at 1
613 km resolution.

614 There are mutual feedbacks between snow and albedo. During snowfall and over the
615 subsequent snowmelt period, snow depth and age affect changes in the albedo. The
616 changes in albedo in turn affect the evolution of snow events by changing the surface
617 energy budget and the proportional distribution of net radiation between turbulent heat
618 and vapor fluxes, and finally by changing the type of precipitation. Our study shows
619 that when the default albedo scheme is replaced by the improved albedo scheme in
620 WRF, the turbulent heat and vapor fluxes estimates increase. The improved scheme
621 significantly outperforms the default Noah scheme for SH estimates, with a reduction
622 (increase) in the RMSE (correlation coefficient) of 10 W m^{-2} (0.1), representing an
623 improvement of 13 % (17 %). The overall accuracy with which WRF estimates
624 turbulent heat and vapor fluxes improves when the improved albedo scheme replaces



625 the default scheme, although there is no significant improvement in LH estimates. This
626 overall improvement leads to a more accurate reproduction of the evolution of snowfall
627 events and to more accurate snow depth estimates. Our study shows that using the
628 improved albedo scheme in WRF reduces the RMSE and increases the correlation
629 coefficient between modeled and observed snow depth, relative to using the default
630 scheme. This improvement is more significant for simulations at 1 km resolution than
631 for simulations at 5 km resolution, with maximum and averaged relative RMSE
632 (correlation coefficient) decreases (increases) of 42 % (367 %) and 21 % (108 %),
633 respectively for 1 km resolution simulations.

634 **Acknowledgements**

635 This research was supported by the Strategic Priority Research Program of Chinese
636 Academy of Sciences (XDA20060101), the Second Tibetan Plateau Scientific
637 Expedition and Research program (STEP) (2019QZKK0103), the National Natural
638 Science Foundation of China (41661144043, 91637312, 41830650, 91737205), MOST
639 High Level Talent grant No. G20190161018, the Chinese Academy of Sciences
640 President's International Fellowship Initiative Grant No. 2020VTA0001, the Key
641 Research Program of Frontier Sciences of Chinese Academy of Sciences (QYZDJ-
642 SSW-DQC019) and Key Research and Development Projects of the Ministry of
643 Science and Technology (2018YFC1505701). The authors express thanks to ECMWF
644 for sharing atmospheric reanalysis data set (ERA5 dataset is available from
645 <https://www.ecmwf.int/en/forecasts/datasets/reanalysis-datasets/era5>), to NASA for
646 offering MODIS reflectance products (<https://modis.gsfc.nasa.gov/>), and to staff from
647 CMA, CAS and Qilian Mountains integrated observatory network for very hard work
648 in meteorological observations and offering the data (CMA meteorological data is
649 available from <http://data.cma.cn/en>; albedo and turbulent heat and vapor fluxes
650 observations from CAS and Qilian Mountains integrated observatory network is
651 provided by National Tibetan Plateau Data Center (<http://data.tpdac.ac.cn>). The first
652 author would like to acknowledge all group members for their help in completing this



653 paper.

654 **Reference**

655 An, Y., Meng, X., Zhao, L., Li, Z., Wang, S., Shang, L., Chen, H., Lyu, S., Li, G., and
656 Ma, Y.: Performance of GLASS and MODIS satellite albedo products in diagnosing
657 albedo variations during different time scales and special weather conditions in the
658 Tibetan Plateau, *Remote Sens.*, 12, 2456, 2020.

659 Aoki, T., Hachikubo, A., and Hori, M.: Effects of snow physical parameters on
660 shortwave broadband albedos, *J. Geophys. Res.*, 108, D19, 2003.

661 Bao, Y. and Lyu, S.: Improvement of surface albedo parameterization within a regional
662 climate model (regcm3), *Hydrol. Earth Syst. Sci.*, 6, 1651-1676, 2009.

663 Bao, Y., Lyu, S., Zhang, Y., Meng, X., and Yang, S.: Improvement of surface albedo
664 simulations over arid regions, *Adv. Atmos. Sci.*, 25, 481-488, 2008.

665 Bloch, M. R.: Dust-induced albedo changes of polar ice sheets and glacierization, *J.*
666 *Glaciol.*, 5, 241-244, 1964.

667 Bonekamp, P. N. J., Collier, E., and Immerzeel, W. W.: The impact of spatial resolution,
668 land use, and spinup time on resolving spatial precipitation patterns in the Himalayas,
669 *J. Hydrometeorol.*, 19, 1565-1581, 2018.

670 Chen, F. and Dudhis, J.: Coupling an advanced land surface-hydrology model with the
671 Penn State-NCAR MM5 modeling system. Part I: Model implementation and
672 sensitivity, *Mon. Weather Rev.*, 129, 569-585, 2001.

673 Collier, E. and Immerzeel, W. W.: High-resolution modeling of atmospheric dynamics
674 in the Nepalese Himalaya, *J. Geophys. Res.*, 120, 9882-9896, 2015.

675 Dang, C., Brandt, R. E., and Warren, S. G.: Parameterizations for narrowband and
676 broadband albedo of pure snow and snow containing mineral dust and black carbon, *J.*



- 677 Geophys. Res., 120, 5446-5468, 2015.
- 678 Dimitrova, R., Silver, Z., Zsedrovits, T., Hocut, C. M., Leo, L. S., Di Sabatino, S., and
679 Fernando, H. J. S.: Assessment of planetary boundary-layer schemes in the Weather
680 Research and Forecasting mesoscale model using Materhorn field data, Bound-Lay
681 Meteorol., 159, 589-609, 2016.
- 682 Ek, M. B., Mitchell, K. E., Lin, Y., Rogers, E., Grunmann, P., Koren, V., Gayno, G., and
683 Tarpley, J. D.: Implementation of Noah land surface model advances in the National
684 Centers for Environmental Prediction operational mesoscale Eta model, J. Geophys.
685 Res., 108, D22, 2003.
- 686 Gao, Y., Xu, J., and Chen, D.: Evaluation of WRF mesoscale climate simulations over
687 the Tibetan Plateau during 1979-2011, J. Clim., 28, 2823-2841, 2015.
- 688 Gardner, A. S. and Sharp, M. J.: A review of snow and ice albedo and the development
689 of a new physically based broadband albedo parameterization, J. Geophys. Res., 115,
690 F1, 2010.
- 691 Hansen, J. and Nazarenko, L.: Soot climate forcing via snow and ice albedos, PNAS,
692 101, 423-428, 2004.
- 693 He, C., Takano, Y., Liou, K.-N., Yang, P., Li, Q., and Chen, F.: Impact of snow grain
694 shape and black carbon-snow internal mixing on snow optical properties:
695 Parameterizations for climate models, J. Clim., 30, 10019-10036, 2017.
- 696 He, C., Liou, K.-N., and Takano, Y.: Resolving size distribution of black carbon
697 internally mixed with snow: Impact on snow optical properties and albedo, Geophys.
698 Res. Lett., 45, 2697-2705, 2018a.
- 699 He, C., Liou, K.-N., Takano, Y., Yang, P., Qi, L., and Chen, F.: Impact of grain shape
700 and multiple black carbon internal mixing on snow albedo: Parameterization and
701 radiative effect analysis, J. Geophys. Res., 123, 1253-1268, 2018b.



- 702 Horvath, K., Koracin, D., Vellore, R., Jiang, J., and Belu, R.: Sub-kilometer dynamical
703 downscaling of near-surface winds in complex terrain using WRF and MM5 mesoscale
704 models, *J. Geophys. Res.*, 117, D11, 2012.
- 705 Jonsell, U., Hock, R., and Holmgren, B.: Spatial and temporal variations in albedo on
706 Storglaciaren, Sweden, *J. Glaciol.*, 49, 59-68, 2003.
- 707 Kuipers Munneke, P., van den Broeke, M. R., Lenaerts, J. T. M., Flanner, M. G.,
708 Gardner, A. S., and van de Berg, W. J.: A new albedo parameterization for use in climate
709 models over the Antarctic ice sheet, *J. Geophys. Res.*, 116, D5, 2011.
- 710 Li, X.: Qilian Mountains integrated observatory network: Dataset of Qinghai Lake
711 integrated observatory network (eddy covariance system of Alpine meadow and
712 grassland ecosystem Superstation, 2018), National Tibetan Plateau Data Center, 2019.
- 713 Li, Y. and Hu, Z.: A study on parameterization of surface albedo over grassland surface
714 in the northern Tibetan Plateau, *Adv. Atmos. Sci.*, 26, 161-168, 2009.
- 715 Liang, X., Xu, M., Gao, W., Kunkel, K., Slusser, J., Dai, Y., Min, Q., Houser, P. R.,
716 Rodell, M., Schaaf, C. B., and Gao, F.: Development of land surface albedo
717 parameterization based on Moderate Resolution Imaging Spectroradiometer (MODIS)
718 data, *J. Geophys. Res.*, 110, D11, 2005.
- 719 Lin, P., Wei, J., Yang, Z., Zhang, Y., and Zhang, K.: Snow data assimilation-constrained
720 land initialization improves seasonal temperature prediction, *Geophys. Res. Lett.*, 43,
721 11423-11432, 2016.
- 722 Liu, L.: Diagnostic analysis and numerical simulation of a regional heavy snowfall over
723 the Tibetan Plateau, Doctoral dissertation, Chapter 5, Institute of Tibetan Plateau
724 Research, Chinese Academy of Sciences, Building 3, Courtyard 16, Lincui Road,
725 Chaoyang District, Beijing, China, 2020.
- 726 Liu, L., Ma, Y., Menenti, M., Zhang, X., and Ma, W.: Evaluation of WRF modeling in



- 727 relation to different land surface schemes and initial and boundary conditions: A snow
728 event simulation over the Tibetan Plateau, *J. Geophys. Res.*, 124, 209-226, 2019.
- 729 Liu, S., Che, T., Xu, Z., Ren, Z., Tan, J., and Zhang, Y.: Qilian Mountains integrated
730 observatory network: Dataset of Heihe integrated observatory network (Large aperture
731 scintillometer of Daman Superstation, 2019), National Tibetan Plateau Data Center,
732 2020.
- 733 Livneh, B., Xia, Y., Mitchell, K. E., Ek, M. B., and Lettenmaier, D. P.: Noah LSM snow
734 model diagnostics and enhancements, *J. Hydrometeorol.*, 11, 721-738, 2010.
- 735 Ma, Y., Wang, Y., and Han, C.: Regionalization of land surface heat fluxes over the
736 heterogeneous landscape: from the Tibetan Plateau to the Third Pole region, *Int. J.*
737 *Remote Sens.*, 39, 5872-5890, 2018.
- 738 Ma, Y., Hu, Z., Xie, Z., Ma, W., Wang, B., Chen, X., Li, M., Zhong, L., Sun, F., Gu, L.,
739 Han, C., Zhang, L., Liu, X., Ding, Z., Sun, G., Wang, S., Wang, Y., and Wang, Z.: A
740 long-term (2005-2016) dataset of hourly integrated land-atmosphere interaction
741 observations on the Tibetan Plateau, *Earth Syst. Sci. Data*, 12, 2937-2957, 2020.
- 742 Malik, M. J., van der Velde, R., Vekerdy, Z., and Su, Z.: Improving modeled snow
743 albedo estimates during the spring melt season, *J. Geophys. Res.*, 119, 7311-7331, 2014.
- 744 Maussion, F., Scherer, D., Finkelnburg, R., Richters, J., Yang, W., and Yao, T.: WRF
745 simulation of a precipitation event over the Tibetan Plateau, China-an assessment using
746 remote sensing and ground observations, *Hydrol. Earth Syst. Sci.*, 15, 1795-1817, 2011.
- 747 Meng, C. and Li, H.: Solar radiation partitioning and surface albedo parameterization
748 in the hinterland of Taklimakan Desert, *Adv. Meteorol.*, 1-8, 2019.
- 749 Meng, X., Lyu, S., Zhang, T., Zhao, L., Li, Z., Han, B., Li, S., Ma, D., Chen, H., Ao, Y.,
750 Luo, S., Shen, Y., Guo, J., and Wen, L.: Simulated cold bias being improved by using
751 MODIS time-varying albedo in the Tibetan Plateau in WRF model, *Environ. Res. Lett.*,



- 752 13, 44028, 2018.
- 753 Norris, J., Carvalho, L. M. V., Jones, C., Cannon, F., Bookhagen, B., Palazzi, E., and
754 Tahir, A. A.: The spatiotemporal variability of precipitation over the Himalaya:
755 Evaluation of one-year WRF model simulation, *Clim. Dynam.*, 49, 2179-2204, 2017.
- 756 Oerlemans, J. and Knap, W. H.: A 1 year record of global radiation and albedo in the
757 ablation zone of Morteratschgletscher, Switzerland, *J. Glaciol.*, 44, 231-238, 1998.
- 758 Park, S. and Park, S. K.: Parameterization of the snow-covered surface albedo in the
759 Noah-MP version 1.0 by implementing vegetation effects, *Geosci. Model Dev.*, 9, 1073-
760 1085, 2016.
- 761 Qin, J., Yang, K., Liang, S., Zhang, H., Ma, Y., Guo, X., and Chen, Z.: Evaluation of
762 surface albedo from GEWEX-SRB and ISCCP-FD data against validated MODIS
763 product over the Tibetan Plateau, *J. Geophys. Res.*, 116, D24, 2011.
- 764 Rahimi, S. R., Wu, C., Liu, X., and Brown, H.: Exploring a variable-resolution
765 approach for simulating regional climate over the Tibetan Plateau using VR-CESM, *J.*
766 *Geophys. Res.*, 124, 4490-4513, 2019.
- 767 Rai, A., Saha, S. K., and Sujith, K.: Implementation of snow albedo schemes of varying
768 complexity and their performances in offline Noah and Noah coupled with NCEP
769 CFSv2, *Clim. Dynam.*, 53, 1261-1276, 2019.
- 770 Roupioz, L., Nerry, F., Jia, L., and Menenti, M.: Improved surface reflectance from
771 remote sensing data with sub-pixel topographic information, *Remote Sens.*, 6, 10356-
772 10374, 2014.
- 773 Roupioz, L., Jia, L., Nerry, F., and Menenti, M.: Estimation of daily solar radiation
774 budget at kilometer resolution over the Tibetan Plateau by integrating MODIS data
775 products and a DEM, *Remote Sens.*, 8, 2016.
- 776 Saito, M., Yang, P., Loeb, N. G., and Kato, S.: A novel parameterization of snow albedo



- 777 based on a two-layer snow model with a mixture of grain habits, *J. Atmos. Sci.*, 76,
778 1419-1436, 2019.
- 779 Sellers, P. J., Randall, D. A., Collatz, G. J., Berry, J. A., Field, C. B., Dazlich, D. A.,
780 Zhang, C., Collelo, G. D., and Bounoua, L.: A revised land surface parameterization
781 (SiB2) for atmospheric GCMs. Part I: Model formulation, *J. Clim.*, 9, 676-705, 1996.
- 782 Skamarock, W., Klemp, J. B., Dudhia, J., Gill, D. O., Barker, D. M., Wang, W., and
783 Powers, J. G.: A description of the advanced research WRF version 3, NCAR Technical
784 Note NCAR/TN-475+STR, 2008.
- 785 Singh, J., Singh, N., Ojha, N., Sharma, A., Pozzer, A., Kiran Kumar, N., Rajeev, K.,
786 Gunthe, S. S., and Kotamarthi, V. R.: Effects of spatial resolution on WRF v3.8.1
787 simulated meteorology over the central Himalaya, *Geosci. Model Dev.*, 2020.
- 788 Wang, J., Cui, Y., He, X., Zhang, J., and Yan, S.: Surface albedo variation and its
789 influencing factors over Dongkemadi glacier, central Tibetan Plateau, *Adv. Meteorol.*,
790 852098, 2015.
- 791 Wang, W., Yang, K., Zhao, L., Zheng, Z., Lu, H., Mamtimin, A., Ding, B., Li, X., Zhao,
792 L., Li, H., Che, T., and Moore, J. C.: Characterizing surface albedo of shallow fresh
793 snow and its importance for snow ablation on the interior of the Tibetan Plateau, *J.*
794 *Hydrometeorol.*, 21, 815-827, 2020.
- 795 Wang, Z., Zeng, X., and Barlage, M.: Moderate Resolution Imaging Spectroradiometer
796 bidirectional reflectance distribution function-based albedo parameterization for
797 weather and climate models, *J. Geophys. Res.*, 112, 2007.
- 798 Warren, S. G. and Wiscombe, W. J.: A model for the spectral albedo of snow .II: Snow
799 containing atmospheric aerosols, *J. Atmos. Sci.*, 37, 2734-2745, 1980.
- 800 Wen, J., Su, Z., Tian, H., Shi, X., Zhang, Y., Wang, X., Liu, R., Zhang, T., Kang, Y.,
801 Lyu, S., and Zhang, J.: Advances in observation and modeling of land surface processes



- 802 over the source region of the Yellow River, *Advances in Earth Science*, 26, 575-585,
803 2011.
- 804 Wiscombe, W. J. and Warren, S. G.: A model for the spectral albedo of snow. I: Pure
805 snow, *J. Atmos. Sci.*, 37, 2712-2733, 1980.
- 806 Xu, J. and Shu, H.: Assimilating MODIS-based albedo and snow cover fraction into the
807 common land model to improve snow depth simulation with direct insertion and
808 deterministic ensemble Kalman filter method, *J. Geophys. Res.*, 119, 10684-10701,
809 2014.
- 810 Xue, Y., Houser, P. R., Maggioni, V., Mei, Y. W., Kumar, S. V., and Yoon, Y.:
811 Assimilation of satellite-based snow cover and freeze/thaw observations over high
812 mountain Asia, *Front. Earth Sci.*, 7, 2019.
- 813 Yuan, W., Xu, W., Ma, M., Chen, S., Liu, W., and Cui, L.: Improved snow cover model
814 in terrestrial ecosystem models over the Qinghai-Tibetan Plateau, *Agr. For. Meteorol.*,
815 218, 161-170, 2016.
- 816 Zhang, W. and Gao, Y.: Topographic correction algorithm for remotely sensed data
817 accounting for indirect irradiance, *Int. J. Remote Sens.*, 32, 1807-1824, 2011.
- 818 Zhang, Y., Hoar, T. J., Yang, Z., Anderson, J. L., Toure, A. M., and Rodell, M.:
819 Assimilation of MODIS snow cover through the data assimilation research testbed and
820 the community land model version 4, *J. Geophys. Res.*, 119, 7091-7103, 2014.
- 821 Zhao, C. and Zhang, R.: Cold and Arid Research Network of Lanzhou university (eddy
822 covariance system of Guazhou station, 2019), National Tibetan Plateau Data Center,
823 2020.
- 824 Zhong, E., Li, Q., Sun, S., Chen, W., Chen, S., and Nath, D.: Improvement of a snow
825 albedo parameterization in the snow-atmosphere-soil transfer model: Evaluation of
826 impacts of aerosol on seasonal snow cover, *Adv. Atmos. Sci.*, 34, 1333-1345, 2017.